Numerical Methods in Geotechnical Engineering – Hicks, Brinkgreve & Rohe (Eds)

Implicit implementation of the Prevost model

B. Cerfontaine
Geomechanics and Geological Engineering, Department ArGEnCo, University of Liege, Belgium
FRIA, FRS-FNRS, National Fund for Scientific Research

R. Charlier
Geomechanics and Geological Engineering, Department ArGEnCo, University of Liege, Belgium

ABSTRACT: The Prevost model for cohesionless soils (Prevost 1985) is currently used for the modelling of their cyclic behaviour, especially in earthquake engineering (Zerfa and Loret 2003) and (Yang and Elgamal 2008). It's made of conical yield surfaces that allow for plastic deformations in both loading and unloading. Its non-associated volumetric flow rule can roughly take into account pore pressure build-up and cyclic mobility.

The method of implementation of a constitutive law is a crucial issue (Montáns and Caminero 2007) and (Mira et al. 2009). On one hand the accuracy of the solution must be ensured, especially when a large number of cycles are considered. But on the other hand, the cost of the computation must be minimized which implies step size as large as possible.

In this paper, an implicit implementation of the Prevost model is proposed. The plastic flow rule is computed through a trapezoidal rule, at the time step $n + 1/2$, in order to increase the accuracy. An iterative process has to be solved, due to the implicit formulation. The Jacobian matrix of the internal Newton-Raphson process is computed analytically to enhance efficiency. The algorithm is implemented in the finite element code LAGAMINE that carries out fully-coupled analysis. Simulations of triaxial tests are compared with "exact" solution.

1 INTRODUCTION

The Prevost's model for cohesionless soils is adapted to the modelling of their cyclic behaviour, (Prevost 1985), (Yang and Elgamal 2008) and (Zerfa and Loret 2003). It's able to capture plasticity effects in both loading and unloading, pore water pressure generation and cyclic mobility as well.

Method of implementation of a constitutive law is a crucial issue since it influences its accuracy (Montáns and Caminero 2007), (Mira et al. 2009) and (Ortiz and Popov 1985). A reliable model is of main importance especially when considering a great number of cycles. Moreover, a greater accuracy allows longer time steps and cpu time savings.

In this paper a closest point projection algorithm for integrating the constitutive law is presented. It's based on an implicit Prager hardening rule proposed by (Montáns 2001). A system of non-linear equations has to be solved at each integration point to update the stress state. The compliance tensor is computed numerically.

The subroutine is implemented in the finite element code LAGAMINE that allows for running fully-coupled simulations. "Exact" results are obtained through an explicit integration of the constitutive equations on Matlab. Comparisons between implicit solutions and exact results is carried out in order to assess the accuracy and the robustness of the algorithm.

2 EQUATIONS OF THE PREVOST MODEL

2.1 *Definitions*

The sign convention of soil mechanics is adopted: compressive stresses and strains are positive. The Macauley brackets $\langle\rangle$ are defined according to

$$\langle\beta\rangle = \frac{1}{2} \cdot (\beta + |\beta|) \tag{1}$$

The symbol ":" indicates a dot product between two tensors (in bold characters). For example, if $\boldsymbol{\sigma}$ is the effective (Cauchy) stress tensor, the product $\boldsymbol{\sigma} : \boldsymbol{\sigma} = \sigma_{ij} \cdot \sigma_{ij}$ in index notation. The identity tensor is written $\boldsymbol{\delta}$, then the mean effective stress is defined as $\mathrm{p} = 1/3 \cdot \boldsymbol{\sigma} : \boldsymbol{\delta}$. The deviatoric stress tensor and the invariant of deviatoric stresses are defined through

$$\mathbf{s} = \boldsymbol{\sigma} - \mathrm{p} \cdot \boldsymbol{\delta} \qquad \text{and} \qquad \mathrm{q} = \sqrt{\frac{3}{2} \cdot \mathbf{s} : \mathbf{s}} \tag{2}$$

2.2 *Constitutive equations*

The Prevost model lies within the framework of elasto-plasticity. Constitutive equations are written in incremental form. The equation (3) links the effective stress rate $\dot{\boldsymbol{\sigma}}$ to the elastic deformation rate $\dot{\boldsymbol{\epsilon}} - \dot{\boldsymbol{\epsilon}}^p$

$$\dot{\boldsymbol{\sigma}} = \mathbf{E} : (\dot{\boldsymbol{\epsilon}} - \dot{\boldsymbol{\epsilon}}^p) \tag{3}$$

where $\mathbf{E}$ is the fourth-order tensor of elastic coefficients, $\dot{\boldsymbol{\epsilon}}$ is the total deformation rate and $\dot{\boldsymbol{\epsilon}}^p$ is the plastic deformation rate defined through

$$\dot{\boldsymbol{\epsilon}}^p = \mathbf{P} \cdot \langle \Delta\gamma \rangle \tag{4}$$

$\mathbf{P}$ is a symmetric second-order tensor defining a non-associated plastic potential. The plastic loading function, $\Delta\gamma$, is a scalar that depicts the variation of plastic deformation and is defined in (5)

$$\Delta\gamma = \frac{1}{\mathrm{H}'} \cdot \mathbf{Q} : \dot{\boldsymbol{\sigma}} \tag{5}$$

where $\mathbf{Q}$ is a second-order tensor defining the unit outer normal to the yield surface and H' the plastic modulus associated to this surface.

2.3 *Yield functions*

The model is made of conical nested yield surfaces in principal stress space (Prevost 1985). Their apex is fixed at the origin of axes but could be translated on the hydrostatic axis to take cohesion into account if necessary. The i-th surface is the locus of the stress states that verify

$$\mathrm{f}^i \equiv \left(\mathbf{s} - \mathrm{p} \cdot \boldsymbol{\alpha}^i\right) : \left(\mathbf{s} - \mathrm{p} \cdot \boldsymbol{\alpha}^i\right) - \frac{2}{3} \cdot \left(\mathrm{p} \cdot \mathrm{M}^i\right)^2 = 0 \tag{6}$$

where $\boldsymbol{\alpha}^i$ is a kinematic deviatoric tensor defining the coordinates of the yield surface centre in deviatoric space and M^i is a material parameter denoting the aperture of the cone. A normal to the yield surface is computed through

$$\begin{aligned} \frac{\partial f}{\partial \boldsymbol{\sigma}} &= 2 \cdot \left(\mathbf{s} - \mathrm{p} \cdot \boldsymbol{\alpha}^i\right) \\ &+ \frac{2}{3} \cdot \left[\mathrm{p} \cdot \left(\boldsymbol{\alpha}^i : \boldsymbol{\alpha}^i - \frac{2}{3} \cdot \left(M^i\right)^2\right) - \mathbf{s} : \boldsymbol{\alpha}^i\right] \cdot \boldsymbol{\delta} \end{aligned} \tag{7}$$

A unit-norm normal tensor is then computed and can be decomposed into deviatoric and volumetric parts as

$$\mathbf{Q} = \frac{\frac{\partial f}{\partial \boldsymbol{\sigma}}}{\left\| \frac{\partial f}{\partial \boldsymbol{\sigma}} \right\|} = \mathbf{Q}' + \mathrm{Q}^{"} \cdot \boldsymbol{\delta} \tag{8}$$

2.4 *Plastic flow rule*

The plastic potential $\mathbf{P} = \mathbf{P}' + \mathrm{P}'' \cdot \boldsymbol{\delta}$ is decomposed into its deviatoric part which is associative

$$\mathbf{P}' = \mathbf{Q}' \tag{9}$$

and its volumetric part which is non-associative

$$\mathrm{P}^{"} = \frac{1}{3} \cdot \frac{\bar{\eta}^2 - \eta^2}{\bar{\eta}^2 + \eta^2} \text{ where } \eta = \frac{\sqrt{3/2 \cdot \mathbf{s} : \mathbf{s}}}{\mathrm{p}} = \frac{\mathrm{q}}{\mathrm{p}} \tag{10}$$

The material parameter $\bar{\eta}$ takes into account the phase transformation line defined by Ishihara (Ishihara et al. 1975). This parameter rules the volumetric behaviour and separates the p-q plane into two zones. Stress ratios (η) lower than $\bar{\eta}$ indicate a plastic contractive behaviour whilst the other zone depicts a dilative plastic behaviour.

2.5 *Hardening rule*

The hardening rule of the surfaces is purely kinematic. During loading, the active surface moves up to come into contact with the next one. The relationship between plastic function and kinematic hardening is determined through the consistency condition (Prevost 1985) and leads to

$$\mathrm{p} \cdot \dot{\boldsymbol{\alpha}}^i = \frac{\mathrm{H}'}{\mathbf{Q}' : \boldsymbol{\mu}} \cdot \langle \Delta\gamma \rangle \cdot \boldsymbol{\mu} \tag{11}$$

where $\boldsymbol{\mu}$ is a tensor defining the direction of translation of the active surface in the deviatoric space. At this step, any direction of translation could be used depending on the strategy used to integrate the constitutive law (explicit or implicit). The only requirement is that any surface has to be at most tangential to the next one, at the end of a given step. Overlapping of the surfaces is then avoided. In this paper, an implicit integration is adopted.

3 IMPLICIT IMPLEMENTATION

3.1 *Plastic flow rule*

The plastic potential is computed as follows through a generalized trapezoidal rule,

$$\mathbf{P}_{n+\alpha} = (1 - \alpha) \cdot \mathbf{P}_n + \alpha \cdot \mathbf{P}_{n+1}. \tag{12}$$

where n stands for the previous converged step and $\mathrm{n}+1$ is the next step to be computed. A value of α equal to one corresponds to a fully implicit integration whilst α equal to zero corresponds to explicit. In order to improve accuracy of the integration (Ortiz and Popov 1985), α value of $1/2$ is adopted.

3.2 *Hardening vs. yield surface*

A conceptual difference exists between continuous and discrete implicit formulation. In the Prevost's algorithm the elastic region lies within the active surface. Therefore, each time a new surface is activated, elastic region changes in size, and the outermost surface drives the algorithm. This topic is addressed in (Caminero and Montáns 2006) and a solution is to distinguish between yield and hardening surfaces.

In the proposed algorithm, yield surface is the innermost one and size of the elastic zone keeps constant. Other surfaces are hardening ones that only influence plastic deformation through plastic moduli. Hence the algorithm is driven by the innermost surface.

3.3 *Implicit scheme*

The implicit discrete scheme is based on the classical plasticity theory based on the return-mapping algorithm, *i.e.* backward Euler, (Simo and Hughes 1998). Combining equations (3), (4) and (5) leads to

$$\dot{\boldsymbol{\sigma}} = \mathbf{E} : \dot{\boldsymbol{\epsilon}} - \mathbf{E} : \mathbf{P} \cdot \Delta\gamma \tag{13}$$

which is rewritten using the concept of elastic predictor $\boldsymbol{\sigma}^{tr} = \boldsymbol{\sigma}_n + \mathbf{E} : \dot{\boldsymbol{\epsilon}}$

$$\boldsymbol{\sigma}_{n+1} - \cancel{\boldsymbol{\sigma}_n} = \boldsymbol{\sigma}^{tr} - \cancel{\boldsymbol{\sigma}_n} - \mathbf{E} : \mathbf{P}_{n+1/2} \cdot \Delta\gamma_{n+1} \tag{14}$$

This equation is decomposed into its deviatoric (15) and volumetric (16) parts

$$\mathbf{s}_{n+1} = \mathbf{s}^{tr} - 2 \cdot \mathrm{G} \cdot \Delta\gamma_{n+1} \cdot \mathbf{Q}'_{n+1/2} \tag{15}$$

$$\mathrm{p}_{n+1} = \mathrm{p}^{tr} - 3 \cdot \mathrm{B} \cdot \mathrm{P}^{"}_{n+1/2} \cdot \Delta\gamma_{n+1} \tag{16}$$

The consistency condition (6) must be enforced at the end of the step $(n+1)$ if plastic loading occurs $(\Delta\gamma_{n+1} > 0)$. A discrete counterpart of this equation is written as follows

$$f_{n+1} \equiv \left(\mathbf{s}_{n+1} - \mathrm{p}_{n+1} \cdot \boldsymbol{\alpha}^1_{n+1}\right) : \hat{\mathbf{n}}_{n+1/2} - \mathrm{p}_{n+1} \cdot \sqrt{\frac{2}{3}} \cdot M^1 = 0 \tag{17}$$

where

$$\hat{\mathbf{n}}_{n+1/2} = \frac{\mathbf{s}^{tr} - \mathrm{p}_{n+1} \cdot \boldsymbol{\alpha}^1_n + \mathbf{s}_n - \mathrm{p}_n \cdot \boldsymbol{\alpha}^1_n}{\|\mathbf{s}^{tr} - \mathrm{p}_{n+1} \cdot \boldsymbol{\alpha}^1_n + \mathbf{s}_n - \mathrm{p}_n \cdot \boldsymbol{\alpha}^1_n\|} \tag{18}$$

is the outer normal to the yield surface computed at mid-step. The Prager's rule drives the kinematical hardening of the yield surface

$$\boldsymbol{\alpha}^1_{n+1} = \boldsymbol{\alpha}^1_n + \frac{\Delta\gamma^1_{n+1}}{\mathrm{p}_{n+1}} \cdot \mathrm{H}^*_{1,n+1} \cdot \hat{\mathbf{n}}_{n+1/2} \tag{19}$$

where $\mathrm{H}^*_{1,n+1}$ is computed according to (11)

$$\mathrm{H}^*_{1,n+1} = \frac{\mathrm{H}'_1}{\mathbf{Q}'_{n+1/2} : \hat{\mathbf{n}}_{n+1/2}}, \tag{20}$$

$\Delta\gamma^1_{n+1}$ is the plastic multiplicator associated to the yield surface and $\mathbf{Q}'_{n+1/2} = \|\mathbf{Q}'_{n+1/2}\| \cdot \hat{\mathbf{n}}_{n+1/2}$.

If the yield surface doesn't overlap any hardening surface, then $\Delta\gamma_{n+1} = \Delta\gamma^1_{n+1}$. A solution that satisfies (15), (16), (17) and (19) has to be found. However, if other surfaces are overlapped, Prager's rule cannot be used alone. Classical Mroz rule currently employed requires an explicit partitioning of the step, which is avoided here. The implicit Prager translation rule proposed in (Montáns 2001) is adopted instead.

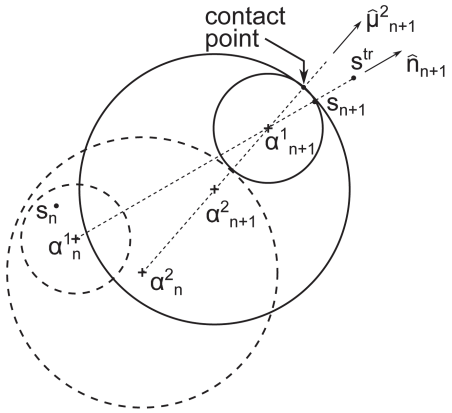

Figure 1. Step 2: elastic predictor ($\mathbf{s}^{tr}$), new position of yield surface ($\boldsymbol{\alpha}^1_{n+1}$), normal to the yield surface ($\hat{\mathbf{n}}_{n+1/2}$), direction of hardening of surface nb. 2 ($\hat{\mathbf{m}}^2_{n+1}$), new position of surface nb. 2 ($\boldsymbol{\alpha}^2_{n+1}$).

The position of each activated surface is computed from the final (at step $n+1$) position of the yield surface. Let "a" be the outermost activated surface, such that

$$\|\boldsymbol{\alpha}^{a+1}_n - \boldsymbol{\alpha}^1_{n+1}\| \leq M^{a+1} - M^1$$

$$\text{and} \quad \|\boldsymbol{\alpha}^a_n - \boldsymbol{\alpha}^1_{n+1}\| > M^a - M^1. \tag{21}$$

For any hardened surface $1 < i \leq a$, the hardening direction is computed recursively from the position of surface $i-1$ (see in Figure 1).

$$\hat{\boldsymbol{\mu}}^i_{n+1} = \frac{\boldsymbol{\alpha}^{i-1}_{n+1} - \boldsymbol{\alpha}^i_n}{\|\boldsymbol{\alpha}^{i-1}_{n+1} - \boldsymbol{\alpha}^i_n\|}. \tag{22}$$

Hence the update of the final position of the surface "i" is defined to avoid overlapping

$$\boldsymbol{\alpha}^i_{n+1} = \boldsymbol{\alpha}^{i-1}_{n+1} + \left(M^{i-1} - M^i\right) \cdot \hat{\boldsymbol{\mu}}^i_{n+1}. \tag{23}$$

This procedure is easily implemented in a constitutive integration subroutine (see Algorithm 1, after (Montáns 2001)). Each component of the consistency parameter associated with hardening surface "i" is computed through

$$\Delta\gamma^i_{n+1} = \mathrm{p}_{n+1} \cdot \frac{\|\boldsymbol{\alpha}^i_{n+1} - \boldsymbol{\alpha}^i_n\|}{\bar{H}^i} \cdot \left\langle \mathbf{Q}'_{n+1/2} : \hat{\boldsymbol{\mu}}^i_{n+1} \right\rangle \tag{24}$$

where $\langle \mathbf{Q}'_{n+1/2} : \hat{\boldsymbol{\mu}}^i_{n+1} \rangle$ allows for convexity of the function $\Delta\gamma(\Delta\epsilon)$ in every condition (Montáns and Caminero 2007), enforces that only hardening in the direction $\hat{\mathbf{n}}_{n+1/2}$ is taken into account and

$$\frac{1}{\bar{H}^i} = \frac{1}{H'^i} - \frac{1}{H'^{i-1}} \tag{25}$$

The consistency parameter is finally computed as the sum of each component

$$\Delta\gamma = \sum_{i=1}^{a} \Delta\gamma^i_{n+1}. \tag{26}$$

Algorithm 1 Computation of $\Delta\gamma_{n+1}$

$\alpha^1_{n+1} = \alpha^1_n + \dfrac{\Delta\gamma^a_{n+1}}{\mathrm{p}_{n+1}} \cdot H^*_{a,n+1} \cdot \hat{\mathbf{n}}_{n+1/2}$
$\mathrm{i} = 1$; TEST $= 1$; $\bar{\boldsymbol{\alpha}} \leftarrow \boldsymbol{\alpha}^1_{n+1}$
while TEST >0 **do**
  $\mathrm{i} = \mathrm{i} + 1$
  TEST $= \|\bar{\boldsymbol{\alpha}} - \boldsymbol{\alpha}^i_n\| - M^i + M^{i+1}$
  if TEST > 0 **then**
    $\hat{\boldsymbol{\mu}}^i_{n+1} = \dfrac{\bar{\boldsymbol{\alpha}} - \boldsymbol{\alpha}^i_n}{\|\bar{\boldsymbol{\alpha}} - \boldsymbol{\alpha}^i_n\|}$
    $\bar{\boldsymbol{\alpha}} \leftarrow \bar{\boldsymbol{\alpha}} + (M^{i-1} - M^i) \cdot \hat{\boldsymbol{\mu}}^i_{n+1}$
    $\Delta\gamma^i_{n+1} = \mathrm{p}_{n+1} \cdot \dfrac{\|\bar{\boldsymbol{\alpha}} - \boldsymbol{\alpha}^i_{n+1}\|}{\bar{H}^i} \cdot \left\langle \mathbf{Q}'_{n+1/2} : \hat{\boldsymbol{\mu}}^i_{n+1} \right\rangle$
  end if
endwhile

Table 1. Material parameters: initial position of the surfaces ($\alpha = \alpha_{11} - \alpha_{33}$), aperture of the surfaces (M), plastic moduli associated (H′), shear modulus (G), bulk modulus (K), slope of the phase transformation line ($\bar{\eta}$).

Surf. Nb.	1	2	3	4	5
α [–]	0.100	0.050	0.100	0.175	0.260
M [–]	0.080	0.150	0.300	0.425	0.640
H′ [MPa]	150	100	30	10	2
Surf. Nb.	6	7	8	9	
α [–]	0.2250	0.220	0.155	0.140	
M [–]	0.775	0.920	1.045	1.140	
H′ [MPa]	1	0.4	0.15	0.01	
G [MPa]			40		
K [MPa]			66.7		
$\bar{\eta}$			0.8		

3.4 *Algorithm for constitutive integration*

The purpose of the algorithm is to compute final stress state $\boldsymbol{\sigma}_{n+1}$ and consistent tangent operator $\mathbb{C}_{n+1}$ for a given increment of deformations $\Delta\boldsymbol{\epsilon}$, where $\mathbb{C}_{n+1}$ is computed by perturbations

$$\mathbb{C}_{n+1} = \frac{\partial \boldsymbol{\sigma}_{n+1}}{\partial \boldsymbol{\epsilon}_{n+1}}. \tag{27}$$

A closest-point projection algorithm is adopted, (Simo and Hughes 1998). The implicit formulation entails a Newton-Raphson process to compute iteratively $\boldsymbol{\sigma}_{n+1}$. Two basic variables are chosen to describe the final stress state: $\Delta\gamma^1_{n+1}$ and p_{n+1}. In order to gain computation time, Jacobian matrix of the local iterative process is computed analytically. For that purpose, two new unknowns are added: $\|\mathbf{Q}'_{n+1/2}\|$ and $\mathrm{H}^*_{1,n+1}$ inspired by (Mira et al. 2009). Four corresponding residuals are defined at step $\mathrm{n}+1$ through

$$r_{1,n+1} \equiv \frac{H^*_{1,n+1}}{\bar{H}^1} \cdot \|\mathbf{Q}'_{n+1/2}\| - 1 \tag{28}$$

$$r_{2,n+1} \equiv \left(\mathbf{s}^{tr}_{n+1} - \mathrm{p}_{n+1} \cdot \boldsymbol{\alpha}^1_n\right) : \hat{\boldsymbol{n}}_{n+1/2} - \sqrt{\frac{2}{3}} \cdot \mathrm{p}_{n+1} \cdot M^1 - 2 \cdot \mathrm{G} \cdot \Delta\gamma_{n+1} \cdot \|\mathbf{Q}'_{n+1/2}\| - \Delta\gamma^1_{n+1} \cdot H^*_{1,n+1} \tag{29}$$

$$r_{3,n+1} \equiv \mathrm{p}_{n+1} - p^{tr} + 3 \cdot B \cdot \Delta\gamma_{n+1} \cdot P^{"}_{n+1/2} \tag{30}$$

$$r_{4,n+1} \equiv \|\mathbf{Q}'_{n+1/2}\| - 2 \cdot \frac{\|\mathbf{s}_{n+1} - \mathrm{p}_{n+1} \cdot \boldsymbol{\alpha}^1_{n+1}\|}{\left\|\dfrac{\partial f}{\partial \sigma}\right\|} \tag{31}$$

4 RESULTS

When dealing with numerical modelling, concepts of verification, validation, efficiency and robustness are of main importance (Brinkgreve 2013). Validation ensures that mathematical model is able to reproduce reality. This step is out of the scope of this paper but interested reader should be referred to (Yang and Elgamal 2008), (Zerfa and Loret 2003) and (Cerfontaine et al. 2013).

Main results presented in this paper concern verification of the implicit algorithm, *i.e.* verifying that algorithm implemented corresponds to continuous mathematical model. Equations of the model are strongly simplified for triaxial tests and an explicit integration of these is carried out in Matlab for very small step sizes. Three examples of stress paths are provided here: monotonic drained, monotonic undrained and cyclic undrained triaxial tests.

4.1 *Material parameters*

Material parameters are obtained for a 60% relative density Nevada Sand, (Arulmoli et al. 1992). Calibration is carried out using simplified equations for triaxial tests (Cerfontaine et al. 2013) and final parameters are carried out in Table 1.

4.2 *Drained monotonic triaxial test*

Results for the drained triaxial tests are given in Figures 2 and 3. Implicit computed solution matches pretty well the exact solution even for large step sizes up to 0.5 %. The internal Newton-Raphson process has most of the time a quadratic rate of convergence, thanks to analytical computation of derivatives and sufficiently accurate initial guess of the solution (Mira et al. 2009).

However, it's worth noting that internal Newton-Raphson process may encounter convergence difficulties for large time steps. Actually, elastic predictor is very huge and initial guesses might be not close enough to the true solution. Then time step has to be reduced (see in Figure 2).

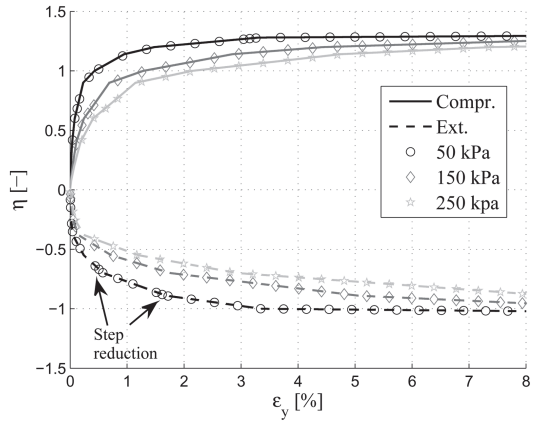

Figure 2. Comparison between implicit algorithm (markers) and explicit computation (continuous for compression or dashed for extension) of a drained monotonic triaxial test for three initial confining pressures (50–150–250 kPa).

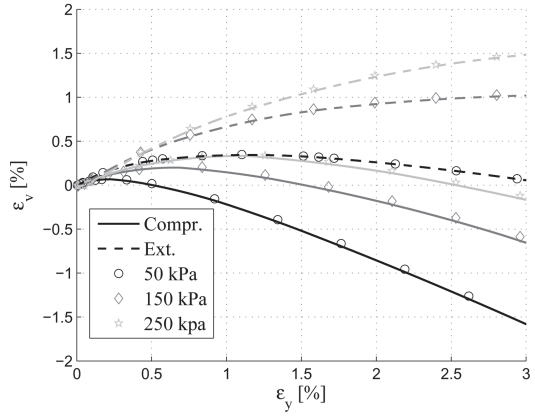

Figure 3. Comparison between implicit algorithm (markers) and explicit computation (continuous for compression or dashed for extension) of a drained monotonic triaxial test for three initial confining pressures (50–150–250 kPa). Zoom on the $\epsilon_v - \epsilon_y$ curve.

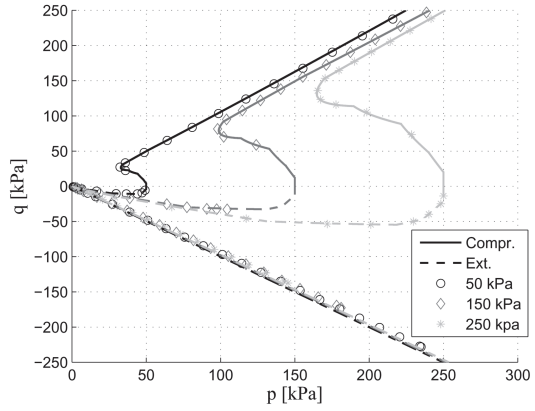

Figure 4. Comparison between implicit algorithm (markers) and explicit computation (continuous for compression or dashed for extension) of an undrained monotonic triaxial test for three initial confining pressures (50–150–250 kPa).

4.3 *Undrained monotonic triaxial test*

Stress paths in the p-q plane for undrained triaxial tests might be very different in compression and extension. In the former case, the stress path is pretty well reproduced (see in Figure 4).

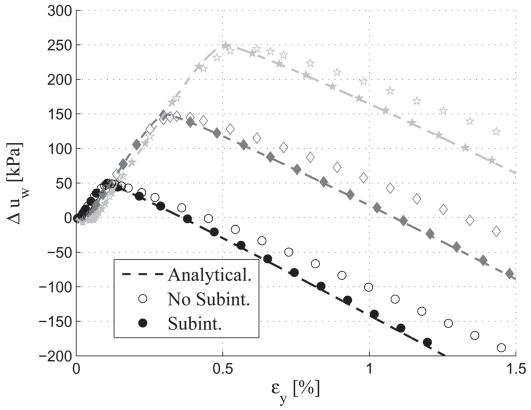

Figure 5. Comparison between implicit algorithm (markers) and explicit computation (dashed) of an undrained monotonic triaxial test in extension for three initial confining pressures (50–150–250). Filled markers in stand for computation with sub-integration.

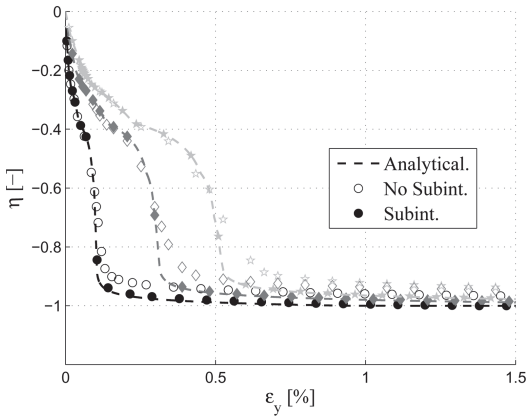

Figure 6. Comparison between implicit algorithm (markers) and explicit computation (dashed) of an undrained monotonic triaxial test in extension for three initial confining pressures (50–150–250 kPa). Filled markers stand for computation with sub-integration.

In the latter one, instabilities and an "elbow" can appear. Even if the stress path seems to be more or less reproduced, the plot of pore water pressure clearly shows that the implicit curve diverges (see in Figure 5). The origin lies in the Figure 6. During the unstable phase of the loading (decreasing |q| and weak p, the soil encounters a very strong variation of η over a small deformation increment. Due to the strong non-linearity of the volumetric plastic potential, P′, the evolution of p is badly approximated and solution diverges. The only possibility to overcome this drawback is to reduce the step size or to subintegrate, (Sloan 1987). The implicit curves with sub-integration are given in Figures 5 and 6.

4.4 *Undrained cyclic triaxial test*

Implicit model is able to reproduce cyclic loading of soil (Figures 7 and 8). This loading implies stress reversal as well as increasing pore water pressure. These behaviours are well-reproduced but the price to pay is a small enough stime step to well capture the decreasing mean effective stress.

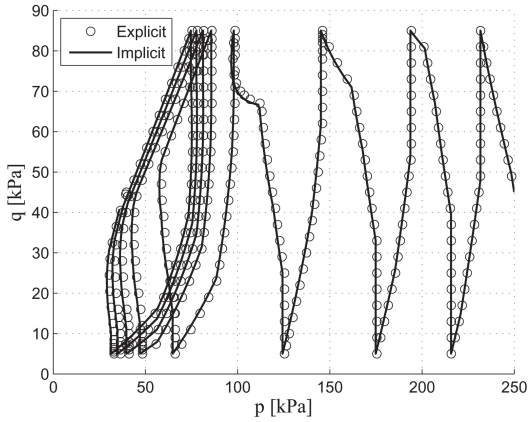

Figure 7. Comparison between implicit algorithm (markers) and explicit computation (continuous) of an undrained cyclic triaxial test.

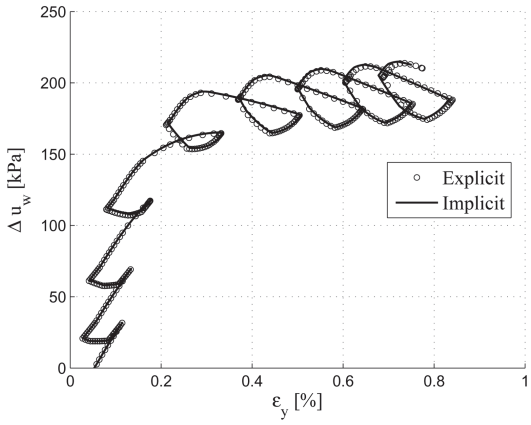

Figure 8. Comparison between implicit algorithm (markers) and explicit computation (continuous) of an undrained cyclic triaxial test.

5 CONCLUSIONS

An implicit implementation of the Prevost's model in the finite element code LAGAMINE was presented in this paper. The integration of the constitutive law is based on a closest-point projection algorithm. Direction of plastic return is computed at the time step $n + 1/2$ in order to improve accuracy of the algorithm. Due to the implicit strategy, a four-unknown local Newton-Raphson procedure has to be performed.

Three different types of tests are used to compare an "exact" solution to implicit algorithm. Results match pretty well exact solution even if some non convergence of the code has been sometimes observed. The most critical problem occurs for undrained extension tests in the nearly liquefied zone. This drawback could be easily overcame by use of subintegration.

ACKNOWLEDGEMENTS

The authors acknowledge the national fund for scientific research for its financial support. The first author would also gratefully thank F.J. Montans for its warm greeting and its shrewd advice.

REFERENCES

Arulmoli, K., K. Muraleetharan, M. Hossain, & L. Fruth (1992). Velacs: Verification of liquefaction analyses by centrifuge studies, laboratory testing program, soil data report. *Research Report*.

Brinkgreve, R. (2013). Validating geotechnical finite element models. In *Proceedings of the 3rd international symposium on computational geomechanics (COMGEO III)*.

Caminero, M. A. & F. J. Montáns (2006, October). An enhanced algorithm for nested surfaces plasticity using the implicit Mróz translation rule. *Computers & Structures 84*(26–27), 1684–1695.

Cerfontaine, B., R. Charlier & F. Collin (2013). Possibilities and limitations of the prevost model for the modelling of cohesionless soil cyclic behaviour. In *Proceedings of the 18th International Conference on Soil Mechanics and Geotechnical Engineering*.

Cerfontaine, B., S. Levasseur & R. Charlier (2013). Axisymmetric transient modelling of a wind turbine foundation in cohesionless soil using the prevost model. *Computational Methods in Marine Engineering*.

Ishihara, K., F. Tatsuoka, & S. Yasuda (1975). Undrained deformation and liquefaction of sand under cyclic stress. *Soils and Foundations 15*, 29–44.

Mira, P., L. Tonni, M. Pastor, & J. A. Fern (2009). A generalized midpoint algorithm for the integration of a generalized plasticity model for sands. *International Journal for Numerical Methods in Geomechanics* (September 2008), 1201–1223.

Montáns, F. (2001). Implicit multilayer j_2 plasticity using prager's translation rule. *International Journal for Numerical Methods in Engineering 50*, 347–375.

Montáns, F. J. & M. a. Caminero (2007). On the consistency of nested surfaces models and their kinematic hardening rules. *International Journal of Solids and Structures 44*(14–15), 5027–5042.

Ortiz, M. & E. P. Popov (1985). Accuracy and stability of integration algorithms for elastoplastic constitutive relations. *International Journal for Numerical Methods in Engineering 21*(9), 1561–1576.

Prevost, J. (1985). A simple plasticity theory for frictional cohesionless soils. *Soil Dynamics and Earthquake Engineering 4*, 9–17.

Simo, J. & T. Hughes (1998). *Computational Inelasticity*. New-York: Springer.

Sloan, S. (1987). Substepping schemes for the numerical integration of elastoplastic stress–strain relations. *International Journal for Numerical Methods in Engineering 24*(5), 893–911.

Yang, Z. & A. Elgamal (2008). Multi-surface cyclic plasticity sand model with lode angle effect. *Geotechnical and Geological Engineering 26*, 335–348.

Zerfa, F. & B. Loret (2003). Coupled dynamic elastic-plastic analysis of earth structures. *Soil Dynamics and Earthquake Engineering 23*(6), 435–454.